Stress-adaptive design of 2D contact interfaces with uniform pressure: A bio-inspired approach

David Hernandez-Aristizabal, Santiago Arroyave-Tobón, Diego Garzon-Alvarado, Jean-Marc Linares

▶ **To cite this version:**

David Hernandez-Aristizabal, Santiago Arroyave-Tobón, Diego Garzon-Alvarado, Jean-Marc Linares. Stress-adaptive design of 2D contact interfaces with uniform pressure: A bio-inspired approach. International Journal of Solids and Structures, 2023, 270, pp.112238. 10.1016/j.ijsolstr.2023.112238 . hal-04069887

HAL Id: hal-04069887
https://hal.science/hal-04069887

Submitted on 14 Apr 2023

HAL is a multi-disciplinary open access archive for the deposit and dissemination of scientific research documents, whether they are published or not. The documents may come from teaching and research institutions in France or abroad, or from public or private research centers.

L'archive ouverte pluridisciplinaire **HAL**, est destinée au dépôt et à la diffusion de documents scientifiques de niveau recherche, publiés ou non, émanant des établissements d'enseignement et de recherche français ou étrangers, des laboratoires publics ou privés.

Stress–adaptive design of 2D contact interfaces with uniform pressure: a bio–inspired approach

David Hernandez–Aristizabal[a,*], Santiago Arroyave–Tobón[a], Diego A. Garzon–Alvarado[b], Jean-Marc Linares[a]

[a]*Aix–Marseille Univ, CNRS, ISM, Marseille, France*
[b]*Departamento de Ingeniería Mecánica y Mecatrónica, Universidad Nacional de Colombia, Bogotá, Colombia*

Abstract

In this article, a bio–mimetic approach to the generative design of contact interfaces with uniform pressure distribution is explored. During the morphogenesis process, biological joints grow depending on the states of stress generating a shape adapted to the mechanical loads. This adaptation is driven by two main rules: shear stress inhibits growth, whereas cyclic hydrostatic compressive stress promotes it. In this work, we demonstrate that the stress–dependent growth rules of synovial joint morphogenesis can be applied to generate contact interfaces with uniform pressure in engineering applications. For that, we present a mathematical model that comprises a contact formulation and a bio–inspired growth function; the model is solved numerically using finite element methods. We analyse the impact of the growth rules of synovial joint development on the contact pressure distribution of two–dimensional contact interfaces. We study the parameter space of the bio–inspired growth function to fine–tune the model parameters. The model is tested in several cases with different boundary conditions and material properties. The results show that the proposed generative design process leads to contact interfaces that provide uniform contact pressure. A quantitative metric of the uniformity of the contact pressure is also defined. This metric indicates that the bio–inspired process generates geometries as good as those obtained with other methods present in the literature without the need of an initial shape close to the final one. Thus, this work demonstrates that synovial joint morphogenesis can be adapted for generative design in engineering.

Keywords: bio–inspired design, generative design, joint morphogenesis, contact interface, stress adaptation

1. Introduction

Synovial joints are characterised by remarkable wear resistance. This performance is attributed to a complex structure that comprises tribological, material, and geometric properties [1]. During morphogenesis, such a structure is formed by a growth process which is influenced not only by chemical but also by mechanical cues [2–4]. For example, in chondrocytes and other cells, mechanical loads can activate integrins—a class of transmembrane proteins that attach to the extracellular matrix—which later activate intracellular signalling pathways that modify the cell activity [5]. In fact, it has been shown that the absence of foetal movement leads to bone and cartilage abnormalities [3, 4]. Hence, synovial joints adapt to mechanical loads as they grow.

This load adaptation is driven by two main rules. Cycles of compressive stress promote chondrocyte proliferation and cartilage repair and maintenance [6, 7]. In contrast, shear stress promotes chondrocyte ossification and cartilage degradation [8, 9]. This means that cyclic compressive stress promotes growth, while shear stress inhibits it and promotes material hardening. The accuracy of these rules has been proven computationally in several works [10–12] where the authors reproduce synovial joint formation.

In mechanical engineering, joints are also common mechanisms for load transfer. They usually undergo dynamic contact loads which expose them to wear. In consequence, material is constantly lost on the surface and the lifetime of these mechanisms is shortened [13]. Further, if the wear rate is not uniformly distributed, certain regions end up being overexposed to material lost and the failure occurs prematurely [14]. Hence, it is convenient to ensure a uniform wear rate.

Wear rate depends on the contact pressure, the material properties and the sliding speed of the bodies in contact [13, 15]. At imposed speeds, contact pressure uniformity is therefore a key factor. Nonetheless, the contact analysis is highly non–linear and presents unexpected phenomena.

Declarations of interest: none
*Corresponding author
E-mail: david.hernandez-aristizabal@univ-amu.fr
Address: 413 AVE Gaston Berger - 13625 Aix-en-Provence, France

For example, the contact between finite cylinders leads to infinite contact pressure at the edges—a phenomenon called edge effect.

In theory, this phenomenon can be reduced by crowning the cylinder along its axial direction. Lundberg [16] investigated this phenomenon and found an analytical expression that leads to uniform contact pressure. Although it is inaccurate close to the edges [17], it has been widely used in engineering and is an important reference profile. For example, it has been used in the shape design of bearing rollers [18, 19] and gear teeth [20]. Nonetheless, since Lundberg's profile is not adequate for many applications—for example when the contact interface does not comprise any flat surface—other strategies have been developed to address this problem, as described below.

With the aim of improving contact pressure distribution several approaches have been investigated. Among them, we can find developments in material properties [21–23], on topology [24–26], on surface texture [27–29] and on shape [30–35]. These works are based on optimisation algorithms following either gradient–based or heuristic strategies. The former requires rigorous mathematical formulations and the computation of derivatives [36]. Although they converge fast, the computation of the gradient may constrain the problem. For example, in [30] the shape of the contour in contact must remain constant, and the optimisation is achieved by modifying the shape of the contours that are not in contact. In addition, gradient–based algorithms are particularly sensitive to the initial guess since they can end up trapped in a local minimum [36]. Concerning heuristic approaches, they can provide almost global solutions, but they usually require a more extensive evaluation of the design space [36]. In addition, for the optimisation of the contact pressure distribution, it is sometimes necessary to impose the general shape of the profile, as done in [19, 34]. Further, when the design variable is the contact profile, the modifications are restricted to local variations [19, 32–35]. In consequence, the designer needs to have a certain knowledge of the form of the target shape. Another approach was proposed in [37, 38] where it was shown the feasibility of applying cartilage growth rules in engineering design. Nonetheless, they did not evaluate the uniformity of the contact pressure distribution and they focused on a particular case.

In this work, we demonstrate that the stress–dependent growth rules of synovial joint morphogenesis can be applied to generate contact interfaces with uniform pressure in engineering applications. We present a mathematical model that comprises a contact formulation and a bio–

inspired growth function. We define a quantitative measure for pressure uniformity to evaluate the obtained contact interfaces. We study the impact of the growth rules of synovial joint development on the contact pressure distribution of two–dimensional contact interfaces. Then, we adapt the growth function for the generative design of contact interfaces and analyse the parameter space to fine–tune the model parameters. The model is tested in several cases with different boundary conditions and material properties.

The rest of the document is organised as follows. The bio–inspired growth model is presented in Section 2 and its numerical approximation in Section 3. In Section 4, we establish an analysis of the parameters to study the behaviour of the growth function and in Section 5 we set up examples to demonstrate the versatility of the methodology. Finally, in Section 6, we examine and discuss the results and in Section 7, we provide the conclusions of the study.

2. Bio–inspired stress–dependent growth function

2.1. Force balance equilibrium for bodies in contact

Synovial joints are formed in a growth process highly dependent on chemical and mechanical stimuli [2]. As a result, they are adapted to both internal and external stimuli. To use this process for industrial applications, we first need to explore the growth forces that generate this adaptation. In particular, the growth forces that are dependent on mechanical cues.

We shall begin with the properties of the desired design. Let us consider a set of $k \in \mathbb{N}$ continuous domains: $\Omega_i \in \mathbb{R}^3$ (where $1 \leq i \leq k$) with closed boundaries: $\Gamma_i = \partial\Omega_i \in \mathbb{R}^3$. Let us also consider that these domains might be: in contact with each other, under external forces and constrained at given points. Thus, each $\Gamma_i = \Gamma_i^c \cup \Gamma_i^f \cup \Gamma_i^d$ where Γ_i^c, Γ_i^f and Γ_i^d are respectively: the contact boundaries, the boundaries where external forces are applied and the constrained boundaries. The force balance equation is then given by [39]:

$$\nabla \cdot \boldsymbol{\sigma}_i(\mathbf{x}) = \mathbf{0} \qquad \forall \mathbf{x} \in \Omega_i, \tag{1}$$

$$\boldsymbol{\sigma}_i(\mathbf{x}) \cdot \mathbf{n}_i(\mathbf{x}) = \mathbf{f}_i(\mathbf{x}) \qquad \forall \mathbf{x} \in \Gamma_i^f, \tag{2}$$

$$\boldsymbol{\sigma}_i(\mathbf{x}) \cdot \mathbf{n}_i(\mathbf{x}) = \mathbf{p}_i(\mathbf{x}) \qquad \forall \mathbf{x} \in \Gamma_i^c, \tag{3}$$

$$\mathbf{u}_i(\mathbf{x}) = \mathbf{u}_i^0(\mathbf{x}) \qquad \forall \mathbf{x} \in \Gamma_i^d, \tag{4}$$

for $1 < i < k$. $\boldsymbol{\sigma}_i$ are stress tensors; $\mathbf{n}_i$ are outward unit vectors; $\mathbf{f}_i$ and $\mathbf{p}_i$ are traction stress vectors related to external forces and contact pressures, respectively; and $\mathbf{u}_i^0$ are fields of fixed displacements.

Our objective is to define Ω_i such that each $\mathbf{p}_i$ has a uniform distribution—in other words, $\partial \mathbf{p}_i / \partial \mathbf{t}_i = 0$ along Γ_i^c, where $\mathbf{t}_i$ are tangent unit vectors to the surfaces Γ_i: $\mathbf{t}_i \cdot \mathbf{n}_i = 0$. To solve this problem, we will use the theory of synovial joint morphogenesis to obtain Ω_i by a process of load adaptation.

Before continuing, let us establish some useful notation. The hydrostatic stress is defined as: $\sigma_{\text{hyd}} = \text{tr}(\boldsymbol{\sigma})/3$. For the shear stress let us use the von Mises stress $\sigma_{\text{v}} = \sqrt{3J_2}$—where J_2 is the second invariant of the deviatoric stress tensor. It will also be useful to write the compressive stress as: σ_{hyc} which is 0 when $\sigma_{\text{hyd}} > 0$ and $-\sigma_{\text{hyd}}$ when $\sigma_{\text{hyd}} < 0$.

2.2. The growth function

As we will use the theory of synovial joint morphogenesis to define Ω_i, let us see the biological growth model. For cellular processes of growth, we can assume that the inertial forces are negligible with respect to viscous and elastic forces [40]. Then, the equilibrium of forces can be written as [40–42]:

$$\nabla \cdot \Big(\boldsymbol{\sigma}_i(\mathbf{x}) + \boldsymbol{\sigma}_g(\mathbf{x}) \Big) = \mathbf{0} \qquad \forall \mathbf{x} \in \Omega_i, \tag{5}$$

where $\boldsymbol{\sigma}_g$ is a stress tensor of growth forces. This tensor is then in charge of the shape adaptation to external loads. In synovial joint formation, this tensor is likely to promote oriented growth as chondrocytes and collagen fibres have different properties and orientations depending on the proximity to the contact region [43]. Near the surface, they are oriented tangentially to the surface. Farther from the surface, they are oriented perpendicularly to the surface [43]. In fact, it has been suggested that such preferential orientation might be related to the direction of principal strains [44]. Thus, growth orientation not only influences the shape but clearly also the mechanical properties of the cartilage, particularly, its anisotropic nature. Nonetheless, in biology, some authors have considered a hydrostatic nature for the growth tensor in computational models and have obtained shapes similar to those seen in nature [10]. Therefore, for this work, we will also

assume hydrostatic growth stress for simplicity. We can then let $\boldsymbol{\sigma}_g = \sigma_g \mathbf{I}$ where $\mathbf{I}$ is the identity matrix.

Research in joint formation indicates that, apart from biochemical cues, growth is controlled by compressive and shear stresses following the next two laws [6–9]: (i) proliferation takes places when chondrocytes are subjected to cyclic compressive stress and (ii) ossification is triggered by shear stress. If we neglect the difference in material properties before and after ossification, we can translate proliferation into growth and ossification into growth inhibition. In short, we can say that cyclic compressive stress prompts growth, while shear stress inhibits it.

To obtain the desired growth function, let us define different combinations of these two basic rules:

- **Scenario I: expansion proportional to compressive stress.** In this situation, we can study the effect of the first biological law in the absence of the second.
- **Scenario II: contraction proportional to compressive stress.** In this situation, we can see the behaviour of the growth process in opposition to the first biological law. This will shed light on how the contact interfaces driven by compressive stress stimuli can be.
- **Scenario III: expansion proportional to compressive stress and inhibited by high shear stress.** In this situation, we can test the evolution of the growth process following the two biological laws.
- **Scenario IV: expansion proportional to compressive stress and inhibited by high shear or high compressive stresses.** In this situation, we propose to enhance the inhibition of the growth. Inhibition will take place not only in the regions with high shear stress but also in regions with high compressive stress. As the distributions of shear and compressive stresses are not the same, this scenario will help us understand which regions should be discouraged from growing.

Since in biology, inhibition is usually imposed by threshold parameters, the following equation describes the proposed scenarios:

$$\sigma_g(\mathbf{x}) = \alpha_g \sigma_{\text{hyc}}(\mathbf{x}) H(\tau_{\text{lim}} - \sigma_{\text{v}}(\mathbf{x})) H(\sigma_{\text{lim}} - \sigma_{\text{hyc}}(\mathbf{x})), \tag{6}$$

where α_g is a parameter referring to the strength of the growth force, τ_{lim} and σ_{lim} are respectively the shear and the compressive stress thresholds, and $H(\varphi)$ is the Heaviside function defined as:

$$H(\varphi) = \begin{cases} 1 & \text{for } \varphi \geq 0, \\ 0 & \text{for } \varphi < 0. \end{cases} \tag{7}$$

Although this type of equation has been successfully used in biology [10], in [37, 38] it was indicated that a discontinuous σ_g as that in Eq. (6) leads to discontinuous growth. Further, this discontinuity also affects the contact pressure distribution. To make Eq. (6) continuous, instead of the Heaviside function, let us use the Sigmoid function which is defined as:

$$S(\varphi) = \frac{1}{1 + \exp(-\upsilon\varphi)}, \tag{8}$$

where υ is a positive parameter. Fig. 1 shows the behaviour of the $S(\varphi_{\text{ref}} - \varphi)$ varying υ and an offset along the φ-axis, φ_{ref}, for $\varphi \in [0, 1]$. As it can be seen in Fig. 1a, as υ approaches zero, S becomes the constant function 0.5. In contrast, as υ approaches infinity, S becomes the Heaviside function. Further, Fig. 1b shows that: for a given υ, there exists a minimum value γ such that for all $\varphi_{\text{ref}} \geq \gamma$, $S(\varphi_{\text{ref}} - \varphi) \approx 1$ for all $\varphi \in [0, 1]$. Similarly, there also exists a maximum value λ such that for all $\varphi_{\text{ref}} \leq \lambda$, $S(\varphi_{\text{ref}} - \varphi) \approx 0$ for all $\varphi \in [0, 1]$. Hence, changing the $H(\cdot)$ by $S(\cdot)$ in Eq. (6) yields:

$$\sigma_g(\mathbf{x}) = \alpha_g \sigma_{\text{hyc}}(\mathbf{x}) S(\tau_{\text{lim}} - \sigma_{\text{v}}(\mathbf{x})) S(\sigma_{\text{lim}} - \sigma_{\text{hyc}}(\mathbf{x})). \tag{9}$$

This function is now continuous; however, the stress magnitude is highly dependent on the magnitude of the external loads. As we want to define a system able to modify the contact shape independent of the stress magnitude, it is necessary to define the growth function in terms of normalised hydrostatic and shear stresses. We propose a normalisation based on the maximum stress values: let $\sigma^*_{\text{hyc}}(\mathbf{x})$ and $\sigma^*_{\text{v}}(\mathbf{x})$ be normalised compressive and shear stresses:

$$\sigma^*_{\text{hyc}}(\mathbf{x}) = \frac{\sigma_{\text{hyc}}(\mathbf{x})}{\max(\sigma_{\text{hyc}})}, \qquad \sigma^*_{\text{v}}(\mathbf{x}) = \frac{\sigma_{\text{v}}(\mathbf{x})}{\max(\sigma_{\text{v}})}.$$

As $\sigma^*_{\text{hyc}}(\mathbf{x}), \sigma^*_{\text{v}}(\mathbf{x}) \in [0, 1]$, the adaptation becomes independent of the stress magnitude—in other words, it only depends on the stress distribution. Using the normalised stresses, the growth force

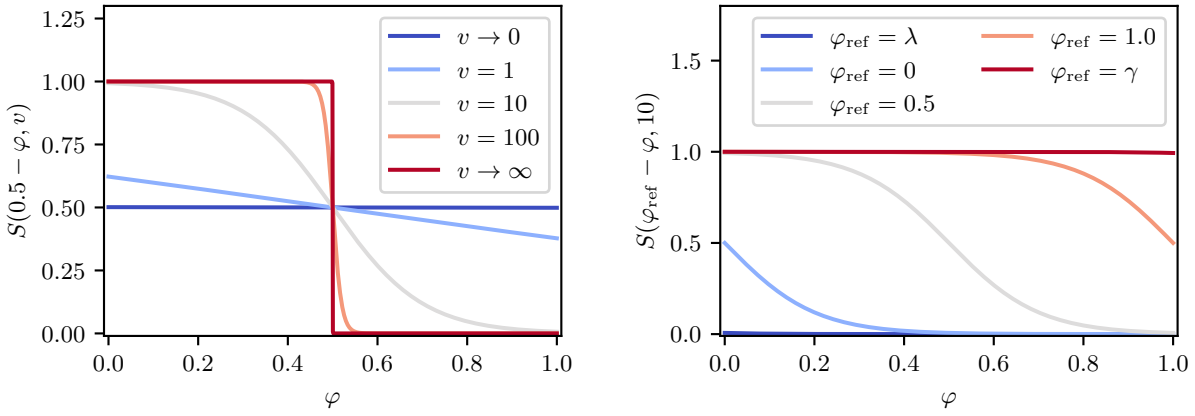

(a) Sigmoid function varying υ.

(b) Sigmoid function varying φ_{ref}.

Figure 1: Sigmoid function response. As υ approaches zero, S becomes the constant function 0.5. In contrast, as υ approaches infinity, S becomes the Heaviside function. Further, for a given υ, there exists a minimum value γ such that for all $\varphi_{\text{ref}} \geq \gamma$, $S(\varphi_{\text{ref}} - \varphi) \approx 1$ for all $\varphi \in [0, 1]$. Similarly, there also exists a maximum value λ such that for all $\varphi_{\text{ref}} \leq \lambda$, $S(\varphi_{\text{ref}} - \varphi) \approx 0$ for all $\varphi \in [0, 1]$.

equation can then be rewritten as:

$$\sigma_g(\mathbf{x}) = \left(\alpha_g \sigma^*_{\text{hyc}}(\mathbf{x}) S\left(\tau^*_{\text{lim}} - \sigma^*_{\text{v}}(\mathbf{x})\right) S\left(\sigma^*_{\text{lim}} - \sigma^*_{\text{hyc}}(\mathbf{x})\right)\right)\beta_g, \tag{10}$$

where τ^*_{lim} and σ^*_{lim} are now dimensionless parameters. β_g has units of pressure to make Eq. (10) compatible with Eq. (5), ~~for this work $\beta_g = 1$GPa~~. The strength of σ_g is now given by the product of β_g and α_g. Thus, we can let α_g be a dimensionless parameter that provides the magnitude and β_g the parameter that contains the units, in this case $\beta_g = 1$GPa. The parameter space for each scenario is shown in Table 1.

Table 1: Parameter space for each scenario of study. In scenario I, we consider uninhibited expansion proportional to hydrostatic compressive stress; in scenario II, uninhibited contraction proportional to hydrostatic compressive stress; in scenario III, expansion proportional to hydrostatic compressive stress and inhibited by high shear stress; and in scenario IV, expansion proportional to hydrostatic compressive stress and inhibited by both high shear and high hydrostatic compressive stresses.

Scenario	α_g	τ^*_{lim}	σ^*_{lim}
I	$(0, +\infty)$	$[\gamma, +\infty)$	$[\gamma, +\infty)$
II	$(-\infty, 0)$	$[\gamma, +\infty)$	$[\gamma, +\infty)$
III	$(0, +\infty)$	$(0, \gamma)$	$[\gamma, +\infty)$
IV	$(0, +\infty)$	$(0, \gamma)$	$(0, \gamma)$

2.3. *The material constitutive law*

As the purpose of this work is to study adaptation in an engineering context, it is reasonable to consider a linear elastic model. Therefore, the stress–strain relation is given by:

$$\boldsymbol{\sigma}(\mathbf{x}) = \frac{E}{1+\nu}\left(\boldsymbol{\varepsilon}(\mathbf{x}) + \frac{\nu}{1-2\nu}\mathrm{tr}\boldsymbol{\varepsilon}(\mathbf{x})\right), \tag{11}$$

where E and ν are Young's modulus and Poisson's ratio, respectively, and $\boldsymbol{\varepsilon}(\mathbf{x}) = 0.5\left(\nabla\mathbf{u}(\mathbf{x}) + (\nabla\mathbf{u}(\mathbf{x}))^{\top}\right)$ is the linear strain tensor.

It would be possible to use the properties of biological materials. Although this would be closer to synovial joint development, the adaptation might be biased by stress fields that do not represent the engineering context. In addition, even in biology, linear elastic models have been used to reproduce synovial joint and bone formation [10–12].

3. A bio–inspired shape–design methodology

We propose an iterative design process that allows us to replicate cyclic compressive stresses. Each cycle is divided into a stress computation step and a growth step. For the stress computation, we need to solve Eqs. (1) to (4)and, for the growth step, Eqs. (4) and (5) together with the following boundary condition:

$$\mathbf{u}_i(\mathbf{x}) \cdot \mathbf{n}_i(\mathbf{x}) = 0, \qquad \forall \mathbf{x} \in \Gamma_i^f. \tag{12}$$

In other words, during the growth step, the displacement along Γ_i^f is purely tangential. Then, we redefine Ω_i by applying the computed displacements.

To objectively compare the response of the algorithm using different values of the parameters in Table 1, let us consider a time–like variable, $\hat{t}_m$. As it can be seen in Eq. (10), σ_g is proportional to α_g. This means that the velocity of growth is also proportional to α_g. Therefore, we consider:

$$\hat{t}_m = m|\alpha_g|, \tag{13}$$

where $m \in \mathbb{N}$ is the number of a given iteration, as a time–like measure. For example, if we have two cases, one with $\alpha_g = 1$ and the other with $\alpha_g = 10$, one iteration of the latter is equivalent to ten iterations of the former.

Algorithm 1 Bio–inspired shape–design algorithm.

Input: Geometry: $\Omega_i(0)$ for $1 \leq i \leq k$.
Input: Boundary conditions: $\mathbf{f}_i$ and $\mathbf{u}_i^0$.
Input: Material properties: E_i and ν_i.
Input: Growth function parameters: α_g, τ^*_{lim} and σ^*_{lim}.
Input: Total simulation time: $\hat{t}_f$.
Output: Geometry adapted to the loading conditions: $\Omega_i(t_f)$.

1: $m \leftarrow 1$
2: $\hat{t}_m \leftarrow m|\alpha_g|$
3: **while** $\hat{t}_m < \hat{t}_f$ **do**
4: Compute the stress state that stimulates growth solving Eqs. (1) to (4).
5: Compute the growth stress using Eq. (10).
6: Find the displacement field $\mathbf{u}(\mathbf{x}(\hat{t}_m))$ that satisfies Eqs. (4), (5) and (12).
7: $\mathbf{x}(\hat{t}_{m+1}) \leftarrow \mathbf{x}(\hat{t}_m) + \mathbf{u}(\mathbf{x}(\hat{t}_m))$
8: $m \leftarrow m + 1$
9: $\hat{t}_m \leftarrow m|\alpha_g|$
10: **end while**

Additionally, Eq. (10) also depends on the parameters of inhibition, υ, τ^*_{lim} and σ^*_{lim}. Therefore, if the inhibition region is larger with one set of parameters than with another, the geometry will change more slowly with the former set than with the latter. In order to compare the model response with different parameters, we will make the L_2–norm of the growth function equal to $|\alpha_g|$ at each iteration. In other words, we will use σ_α instead of σ_g defined as:

$$\sigma_\alpha = \frac{|\alpha_g|}{\|\sigma_g\|_{L_2(\cup_i \Omega_i)}} \sigma_g \tag{14}$$

where $\|\cdot\|_{L_2(\cup_i\Omega_i)}$ refers to the L_2–norm in $\cup_i\Omega_i$. The use of Eqs. (13) and (14) allows us to objectively compare the response of the algorithm using different parameters.

Algorithm 1 presents the algorithm to mimic the biological growth process. As can be seen, computing the displacement field (steps 4-6) is quite simple compered to gradient–based algorithms—there are no derivatives to calculate nor surface–dependent variables. The implementation was done using Code_Aster [45] and GMSH [46]. The former was used to solve the equations by finite element methods and the latter was used to control the evolution of the mesh. The computational implementation is available in: https://github.com/sarroyavet/BioDesign_ANR/tree/main/StressAdaptiveDesignOf2D

4. Impact of the parameters on the contact interface

In this section, we will set up a reference case of study to analyse the impacts of the model parameters on the uniformity of the contact pressure. In addition, we will define metrics to measure the performance of the algorithm and the generated contact interfaces. As we will explore different growth scenarios and parameters, we will consider a two–dimensional framework and frictionless contact. In the context of contact analysis, the theory of semi–infinite elastic bodies is widely used [17]. In consequence, we will consider the contact between a half–space and an infinite cylinder that satisfies the state of plane–strain. Further, the consideration of frictional effects significantly augments the computational time. For example, in [47], the authors showed that wear simulations considering friction were up to three times longer than their frictionless counterparts. Even though we are not modelling wear, the process is similar: a calculation of the contact pressure followed by a geometry update. Thus, using a two–dimensional frictionless contact framework will significantly reduce computational time.

We will also limit the growth to only one domain. Thus, the degrees of freedom of the design problem will be reduced to one domain, facilitating the analysis of the adaptation process. This assumption is also reasonable in the engineering context as it would be appropriate to define an easy–to–manufacture geometry and only generate an adapted and complex shape. For example, in the case of roller bearings, it is common to crown the roller profile while letting flat that of the race. Nonetheless, it would be interesting to explore the advantages of allowing both domains grow in future works.

To sum up, in this section, the model and the algorithm will be simplified by the following assumptions: (i) two–dimensional framework where plane–strain conditions are applied, (ii) frictionless contact and (iii) growth applied to only one domain.

4.1. Description of the case of study

Let us consider the contact between two elastic semi–infinite bodies: a cylinder (Ω_1) and a half–space (Ω_2). Let us also apply a load on the cylinder in the normal direction to the surface of the half-space. Since this case satisfies the plane–strain conditions, it can be reduced to a two–dimensional framework, a schematic view is depicted in Fig. 2a. To analyse the adaptation of one

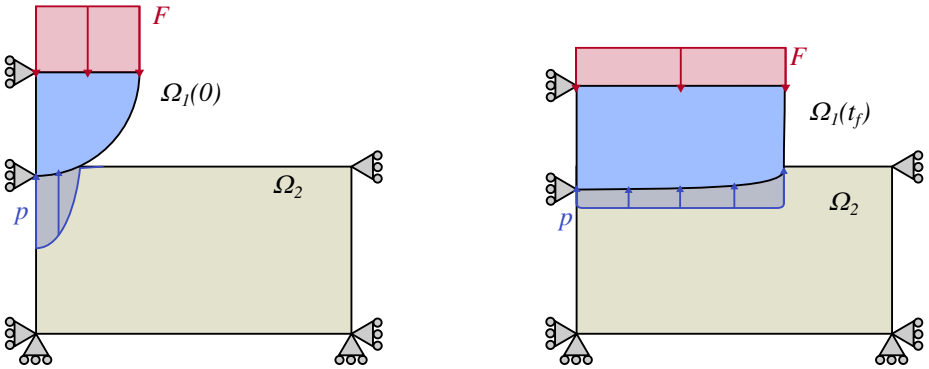

(a) Initial geometry. (b) Final geometry.

Figure 2: Two–dimensional setting of the case of study. Here p refers to the contact pressure along the contact interface and F to the applied force.

Table 2: Geometric parameters of the initial geometries. R, l_i are illustrated in Fig. 3 for both types of geometry.

Geometry	$R[mm]$	l_1[mm]	l_2[mm]	l_3[mm]	l_4[mm]
Circle	4.5	50	18	—	—
Rectangle	0.45	50	18	4.5	4.5

domain keeping the external stimuli untouched, let now the growth be only applied to the cylinder. In other words, let $\sigma_g(\mathbf{x}) = 0$ for all $\mathbf{x} \in \Omega_2$.

The goal of the growth function is to yield a shape to obtain a constant contact pressure. Thus, after the design process, we expect to have a geometry adapted to the load that generates a uniform contact pressure as depicted in Fig. 2b.

4.2. Geometry, material properties and loading conditions

First, let Young's modulus and Poisson's ratio be 210GPa and 0.3, respectively, and let F = 10kN. Regarding the initial cross section of Ω_1, we can define two types depending on the distribution of the initial contact pressure: (i) a higher pressure in the middle of the contact area or (ii) a higher contact pressure at the edges of the contact area. We can use a circle for the former and a rectangle with rounded edges for the latter. Fig. 3 shows a schematic representation of the geometry and Table 2 establishes the values of the dimensions. The load, the material properties and the initial size of the geometries were adapted from the case of study presented in [19].

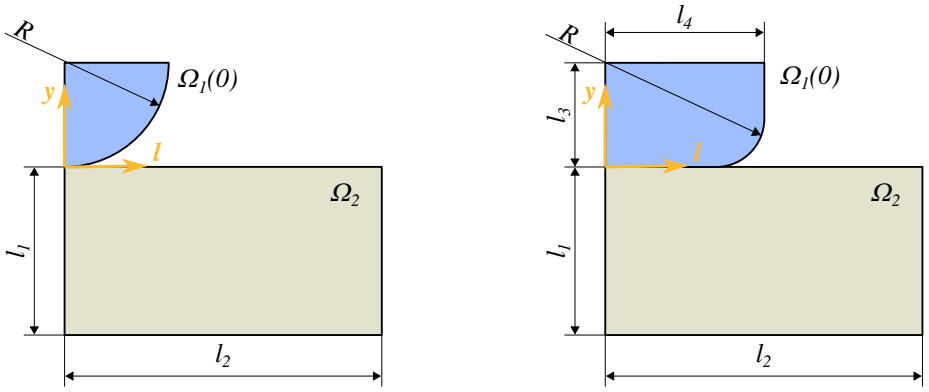

(a) Circular initial geometry.

(b) Rectangular initial geometry.

Figure 3: Geometry of the case of study.

4.3. *Performance evaluation*

To evaluate the performance of the procedure, let us define a measure to qualify the contact pressure distribution. In the best situation, the contact pressure is uniformly distributed and, therefore, all the contact area is properly exploited. Thus, let us define a measure to compare the pressure distribution of a given contact area with an equivalent uniform pressure. Such a measure should be able to tell how close a given pressure distribution is to a uniform distribution. For each $\hat{t}_m$, let $a_c(\hat{t}_m)$ be the contact area and let $p_e(a_c(\hat{t}_m))$ be an equivalent constant pressure given by:

$$p_e(a_c(\hat{t}_m)) = \frac{F}{a_c(\hat{t}_m)}. \tag{15}$$

Now, let us define the pressure distribution quality as:

$$Q_p(\hat{t}_m) = 1 - \frac{\|p_e(a_c(\hat{t}_m)) - p(\hat{t}_m)\|_{L_2(\Gamma_1^c(\hat{t}_m))}}{\|p_e(a_c(\hat{t}_m))\|_{L_2(\Gamma_1^c(\hat{t}_m))} + \|p(\hat{t}_m)\|_{L_2(\Gamma_1^c(\hat{t}_m))}}, \tag{16}$$

where $\|\cdot\|_{L_2(\Gamma_1^c(\hat{t}_m))}$ refers to the L_2-norm in $\Gamma_1^c(\hat{t}_m)$. By means of the triangle inequality [48], we know that $0 \leq Q_p \leq 1$. Additionally, $Q_p \to 1$ as $p \to p_e$ and $Q_p \to 0$ as p concentrates at a specific point. We then look for high values of Q_p. Table 3 indicates the value of Q_p based on the reconstruction of results presented in other works.

Apart from this evaluation at each step, we can also compute the average of Q_p as well as the

Table 3: Evaluation of the pressure distribution quality present in other works based on the reported graphs. We used a plot digitiser tool to compute Q_p.

	Reference	Q_p	Strategy
Contact profile as design variable.	[18] Fig. 4	0.93	Optimisation and approximation of a logarithmic profile.
	[34] Fig. 11	0.95	Optimisation of a super–elliptic profile.
	[32] Fig. 15	0.95	Optimisation of the contact profile.
	The present work	0.96	Bio–inspired generative design.
	[19] Fig. 7	0.99	Optimisation of a logarithmic profile.
Other design variables.	[30] Fig. 6	0.86	Optimisation of the non–in–contact contour.
	[24] Fig. 9	0.94	Optimisation of a predefined topology.
	[23] Fig. 5a	0.94	Optimisation of the material properties.
	[26] Fig. 6b	0.99	Topology optimisation.

average of the maximum contact pressure along the simulation as:

$$\bar{Q}_p = \sum_{m=1}^{m=m_f} \frac{Q_p(\hat{t}_m)}{m_f},$$
$$\bar{p}_{\max} = \sum_{m=1}^{m=m_f} \frac{p_{\max}(\hat{t}_m)}{m_f},$$

with $t_f = |\alpha_g| m_f$, where m_f refers to the last iteration and t_f to the total time. Thus, we can evaluate the consistency of the design process in a general manner.

4.4. Exploration of the design process

As we aim to understand how the growth rules of joint formation can be applied to our case of study, we propose the following pathway. First, we will see the impact of α_g in terms of convergence in both scenarios I and II. From this study, we will define an appropriate value of α_g. Then, we will explore the response of the design process in scenarios III and IV and qualify the contact pressure distribution varying τ^*_{lim}, σ^*_{lim} and υ. Following this exploration, we will select an appropriate combination of parameters and examine the evolution of the design process utilising a rectangle as the initial geometry.

5. Examples of application

In this section, we will present other examples to evaluate the applicability of the bio–inspired growth model after the definition of the parameters. We will consider plane–stress and axisymmet-

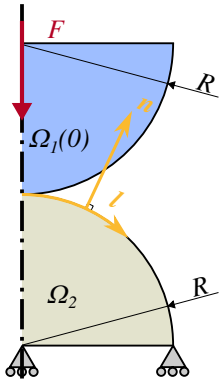

Figure 4: Initial geometry of the axisymmetric case of study. The coordinate system $\boldsymbol{l}$ and $\boldsymbol{n}$ will be used later to define the surface of Ω_1 relative to the surface of Ω_2.

ric conditions and we will change the material properties, the magnitude of the load and the fixed geometry (Ω_2). Further, we will also consider an additional rule to satisfy an additional design requirement.

5.1. Plane–stress and softer material

For this test, let us consider the contact between two thin plates. We shall consider the analogous plane–stress case to the plane–strain case presented in Section 4.1 (see Fig. 3). Nonetheless, let us consider a softer material (for both Ω_1 and Ω_2) with $E = 2$GPa and $\nu = 0.4$—these elastic properties are close to those of some engineering polymers—, $R = 10$mm and $F = 100$N.

5.2. Axial symmetry and geometries with distinct material properties

In this case, let us consider the contact between a soft material for Ω_1 ($E = 2$GPa and $\nu = 0.4$) and a rigid material for Ω_2 ($E = 250$GPa and $\nu = 0.2$) and the initial geometry presented in Fig. 4 with $R = 14$mm and $F = 3000$N. This case represents the loading conditions and material properties of hip–joint prostheses under static analyses [49, 50].

5.3. Additional design requirement: maximum von Mises stress

So far, the design process makes the domain grow indefinitely. This means that we need to include an additional requirement to constrain the growth. It could be a geometric restriction (such as a maximum contact area) or a structural constraint (such as a maximum shear stress). We can combine the growth function in Eq. (10)—whose main objective is to provide a uniform

contact pressure—with a restriction function. Let us then rewrite Eq. (5) as:

$$\nabla \cdot \Big(\boldsymbol{\sigma}(\mathbf{x}) + \eta_g \boldsymbol{\sigma}_g(\mathbf{x}) + \eta_r \boldsymbol{\sigma}_r(\mathbf{x})\Big) = \mathbf{0}, \tag{17}$$

where η_g and η_r are the strengths of the contact pressure improvement and of the restriction, respectively. We can use Q_p to define η_g as:

$$\eta_g = 1 - Q_p. \tag{18}$$

For the definition of $\boldsymbol{\sigma_r}$, let us impose a maximum von Mises stress. First, we can define a von Mises stress quality as:

$$Q_v = 1 - \frac{\max(\sigma_{\mathrm{v}}(\mathbf{x})) - \tau_{\mathrm{ref}}}{\max(\sigma_{\mathrm{v}}(\mathbf{x})) + \tau_{\mathrm{ref}}}, \tag{19}$$

where τ_{ref} is the target von Mises stress of the restriction. As it can be seen, $Q_v \to 1$ as $\max(\sigma_{\mathrm{v}}) \to \tau_{\mathrm{ref}}$, $Q_v < 1$ when $\max(\sigma_{\mathrm{v}}) > \tau_{\mathrm{ref}}$ and $Q_v > 1$ when $\max(\sigma_{\mathrm{v}}) < \tau_{\mathrm{ref}}$. We can also consider $\boldsymbol{\sigma}_r = \mathbf{I}$ (hydrostatic) and

$$\eta_r = \alpha_r(1 - Q_v), \tag{20}$$

where α_r is a positive parameter. As we can see, $\boldsymbol{\sigma}_r$ is space–independent and produces global expansion or contraction. For this case, we will consider the plane–strain case presented in Section 4.

6. Results and discussion

6.1. Convergence

To ensure numerical precision, the contact algorithm was tested with different contact element lengths. For that, the contact pressure was calculated using the circular geometry described above. This case can be analytically solved using Hertz theory [17] in cases where the cylinder diameter is significantly larger than the contact area width. In consequence, we applied a load of 100N so that, according to Hertz theory, the maximum contact pressure is 903.4MPa, and the contact area width is 0.141[mm]. Thus $R \gg a_c$ and the conditions for Hertz theory are satisfied.

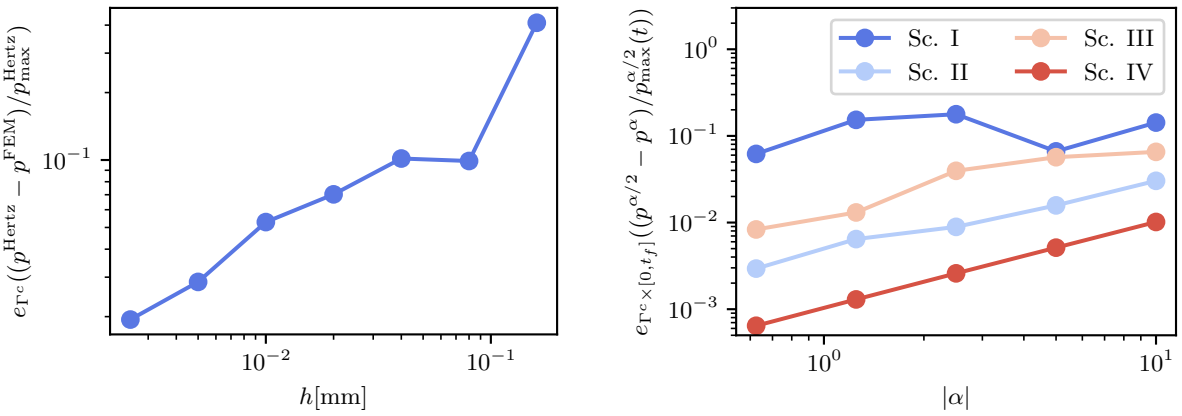

(a) Convergence in h.

(b) Convegence in α_g with $t_f = 500$.

Figure 5: Convergence of the model in mesh size and equivalent time step. In (a) $e_{\Gamma^c}(f) = \sqrt{\int_{\Gamma^c} f(\mathbf{x})^2 d\Gamma^c / \int_{\Gamma^c} d\Gamma^c}$ and in (b) $e_{\Gamma^c\times[0,t_f]}(f) = \sqrt{\int_0^{t_f}\int_{\Gamma^c} f(\mathbf{x},t)^2 d\Gamma^c dt / \int_0^{t_f}\int_{\Gamma^c} d\Gamma^c dt}$ are the L_2–norms of a given function f. In (a) $f = (p^{\text{Hertz}} - p^{\text{FEM}})/p^{\text{FEM}}_{\max})$ which is the normalised error between the contact pressure calculated by Hertz theory and by the finite element method. In (b) $f = (p^{\alpha/2} - p^{\alpha})/p^{\alpha/2}_{\max}(t)$ which is the normalised contact pressure error using as reference a simulation using $\alpha/2$.

Fig. 5a shows the L_2–norm of the normalised difference between the results using Hertz theory and finite elements varying the element length. The normalisation was made with respect to the maximum contact pressure calculated by Hertz theory. It can be seen that as the mesh is refined, the numerical approximation approaches the analytical solution. In addition, for this case, an element length of 0.01mm is sufficient to make the error norm lower than 0.05. Thus, this value was selected for the other simulations.

As indicated in Eq. (13), α_g works as a time step variable. Therefore, the convergence of the algorithm with α_g was also tested. For that, t_f was set to 500—which is large enough to see the behaviour of the design process and to test the convergence. The L_2–norm of the normalised contact pressure between simulations was computed. The normalisation was made by means of the maximum contact pressure at each step. Fig. 5b shows the relative difference among several simulations varying α_g from 0.3125 to 10 for each scenario. We can see that for scenarios II, III and IV, as α_g decreases, such a difference also decreases. Thus, for these scenarios the algorithm is also convergent in terms of α_g—we will take a closer look for scenario I in the following section. We selected $\alpha_g = 1.25$ to study the response of the design process in scenarios III and IV as, for

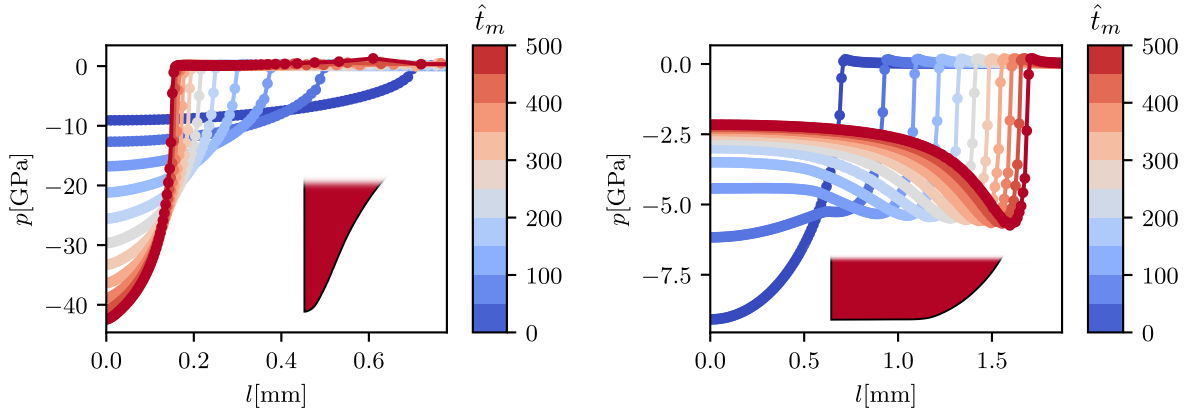

Figure 6: Evolution (from blue to red lines) of the contact pressure along the contact line in scenarios I (a) and II (b) with $|\alpha_g| = 0.3125$. l refers to arc length and the red shapes refer to the geometry of last iteration.

such a value, the error norm is lower than 0.05. For scenarios I and II, we used the simulations with $\alpha_g = 0.3125$, the lowest value used in the convergence analysis.

6.2. The response of the design process in scenarios I and II

Fig. 6a shows the evolution of the contact pressure distribution (from blue to red lines) for scenario I. For this case, it was necessary to add a condition to the mesh such that the number of nodes in contact was always above a given threshold—we used a minimum of 50 nodes. This additional condition was necessary since the contact area was reduced during the simulation. We can see that growing (from blue to red distributions) proportionally to the compressive stress makes a pressure distribution highly concentrated on the initial point of maximum contact pressure. This is a reasonable result given the fact that the maximum compressive stress is located on the surface—more precisely, at the point of maximum contact pressure. Thus, this region grows faster than its neighbours enlarging the curvature. In addition, this curvature increase reduces the contact area and, in consequence, the maximum contact pressure rises. We can say that in the scenario I, the shape tends to have an infinite contact pressure and a zero contact area. This singularity explains the behaviour of the convergence seen in Fig. 5b.

On the other hand, Fig. 6b shows that contraction (from blue to red distributions) in proportion to compressive stress makes the pressure concentrate at the edges. As the pressure changes

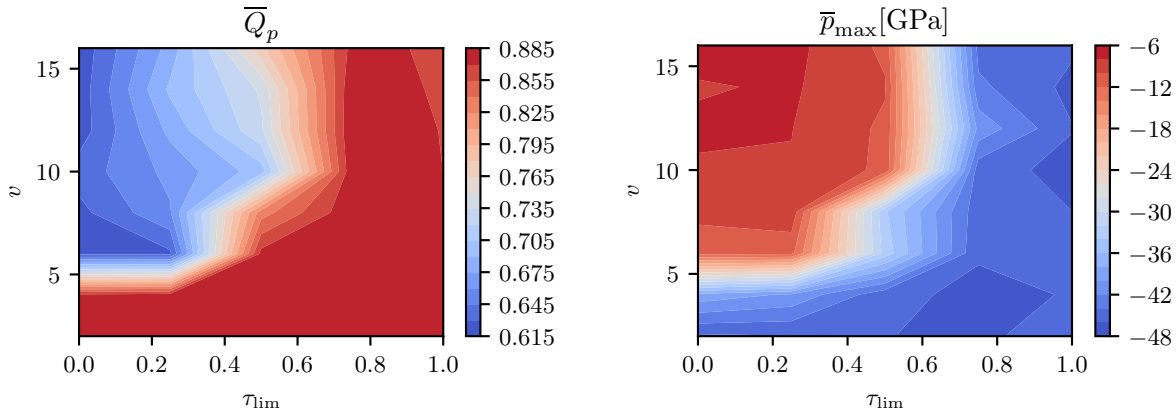

(a) (b)

Figure 7: Response of the design process in scenario III with $t_f = 2000$ in terms of the average of the pressure quality (a) and the average of the maximum contact pressure (b) along the simulation.

from being concentrated in the middle to the edges, the profile flattens and the maximum pressure lowers. However, once the edge effect is formed, the maximum pressure rises ~~.~~ and ~~Additionally, it can also be seen~~ the pressure distribution tends to become singular at the edge. Yet, in the used timescale, this tendency does not affect the convergence with respect to α_g, as can be seen in Fig. 5b. Lastly, we can also see that this contraction also enlarges the contact area.

6.3. Response of the design process in scenarios III and IV

We now know that while growing proportionally to compressive stress decreases the contact area and concentrates the pressure at the middle, contraction proportional to compressive stress increases the contact area and concentrates the pressure at the edges. The former generates geometries that tend to have an infinite curvature at the contact zone, while the latter makes geometries which tend to be flat (zero curvature). Since both scenarios are not desirable, we continued the exploration of the growth rules.

Fig. 7 shows the response of the design process in scenario III. Fig. 7a indicates the average of the pressure quality and Fig. 7b the average of the maximum contact pressure along the simulation. It can be seen that the pressure quality is higher (up to 0.855) at lower values of v or higher values of τ^*_{lim}. However, such a combination almost eliminates the inhibition. As seen in Fig. 1, low values of v and high values of τ^*_{lim} cause S to be almost a constant function. If S becomes a

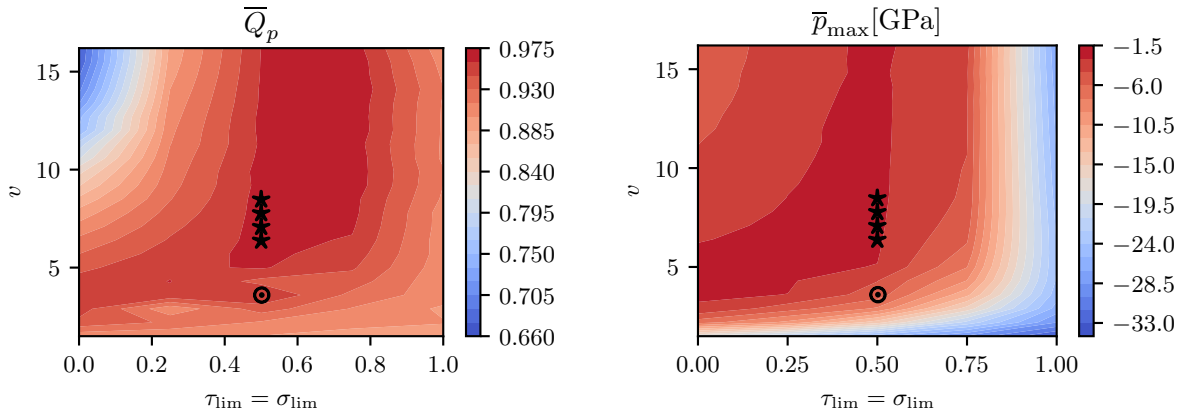

(a) (b)

Figure 8: Response of the design process in scenario IV with $t_f = 2000$ in terms of the average pressure quality (a) and the average of the maximum contact pressure (b) along thee simulation. The $\star$ symbols refer to the best cases. In such cases $\upsilon = 6.4, 7.1, 7.8, 8.5$. The $\odot$ symbol refers to the case with $\upsilon = 3.6$.

constant function, Eq. (10) reduces to $\sigma_g(\mathbf{x}) = c\sigma^*_{\text{hyc}}(\mathbf{x})$, where c is a constant, and no inhibition is present. In fact, we can see in Fig. 7b that the region of higher $\bar{Q}_p$ is also the region of higher contact pressure. This is exactly what happened in the uninhibited growth scenario.

We can also see that, in scenario III, we can not obtain an appropriate result. In both graphs of Fig. 7, the red regions specify the desired results—high pressure quality and low contact pressure. As can be seen, these regions exclude each other—the red region in Fig. 7a intersects with the blue region in Fig. 7b and the other way around—; this justifies the need to modify the growth function.

To address this situation, an additional inhibition was added. The results in scenario I indicate that unrestricted growth proportional to the compressive stress yields extremely high contact pressure. Since the maximum shear stress is not located in the same region as the maximum compressive stress, the region of maximum compressive stress is not always necessarily inhibited. Therefore, the growth force keeps enlarging the curvature around the point of maximum contact pressure. Thus, in scenario IV, the growth force was inhibited by high compressive stress. As a consequence, two new parameters appear σ^*_{lim} and another υ. Yet, we let $\sigma^*_{\text{lim}} = \tau^*_{\text{lim}}$ and let the same υ for both Sigmoid functions of Eq. (10). Fig. 8 shows the response of the design process with the new growth function modifying υ and the stress limits. In Fig. 8a, we see that $\bar{Q}_p$ is

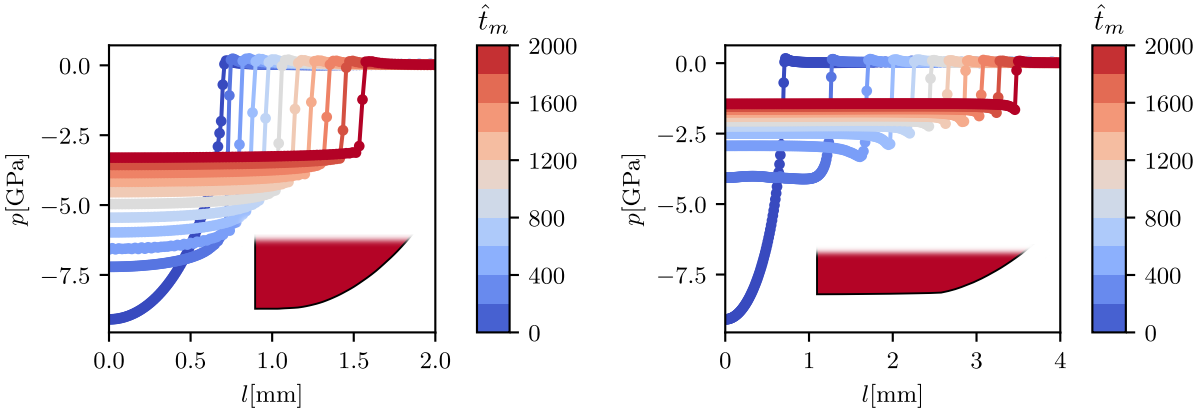

Figure 9: Evolution (from blue to red lines) of the contact pressure along the contact line in scenario IV with $\tau^*_{\text{lim}} = \sigma^*_{\text{lim}} = 0.5$ and de circular initial geometry. $\upsilon = 3.6$ in (a) and $\upsilon = 7.1$ in (b). l refers to arc length and the red shapes refer to the geometry of the last iteration.

significantly greater (up to 0.975) than in the previous scenario. In addition, the zone of higher pressure quality intersects the zone of lower maximum contact pressure—for $\sigma^*_{\text{lim}} = \tau^*_{\text{lim}} = 0.5$ and $\upsilon > 5$. Hence, we see that the added inhibition leads to the desired contact pressure distribution.

Fig. 8 also indicates the best cases by $\star$ (they correspond to $\upsilon = 6.4, 7.1, 7.8, 8.5$). In addition, in Fig. 8a, there is a second local maximum value around $\upsilon = 3.6$ indicated by $\odot$. In order to better understand this situation, Fig. 9 shows the evolution of the contact pressure distribution with $\tau^*_{\text{lim}} = \sigma^*_{\text{lim}} = 0.5$ and $\upsilon = 3.6$ and $\upsilon = 7.1$. In both cases, as the iterations go on, the contact area augments, the maximum contact pressure decreases and the contact pressure distribution flattens. In addition, the pressure quality is high—above 0.96 for $\upsilon = 3.6$ and above 0.97 for $\upsilon = 7.1$. Nonetheless, we can notice an important difference. For $\upsilon = 3.6$, the maximum pressure remains in the centre, while for $\upsilon = 7.1$, it goes to the edges. Thus, the combined inhibition of shear and compressive stresses balances the expansion and contraction present in scenarios I and II. With $\upsilon = 3.6$, the effects in scenario I slightly dominate, while with $\upsilon = 7.1$ the effects in scenario II are somewhat more present. This type of behaviour can also be seen in logarithmic profiles. For example, Cui and He [19] presented a modified Lundberg profile with similar contact pressure distributions. Depending on the combination of parameters, the pressure tends to be concentrated

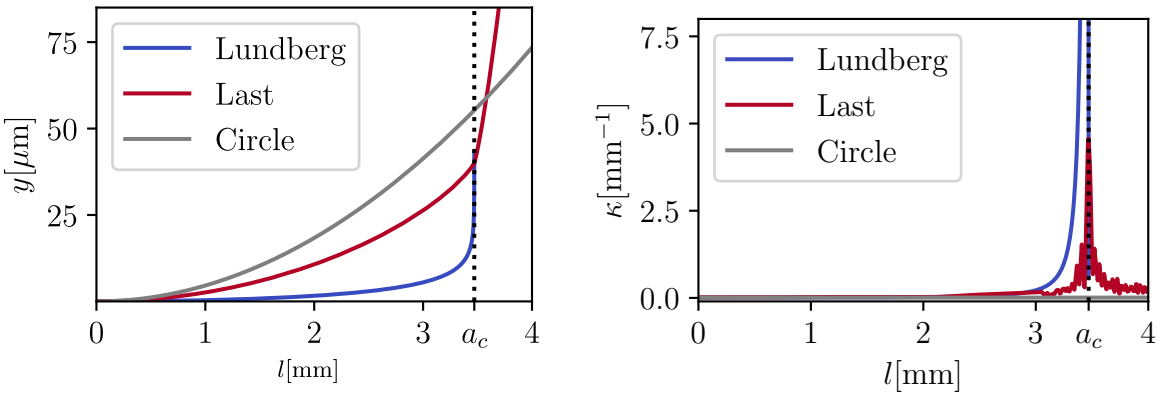

(a) Profile.

(b) Curvature.

Figure 10: Geometric characteristics of the last profile obtained with $\upsilon = 7.1$.

either in the middle or at the edges.

6.4. Geometric properties of the contact interface

In terms of geometry, we can see both the profile and the curvature of the last shape obtained with $\upsilon = 7.1$ in Fig. 10. Fig. 10a shows that the algorithm generates a profile whose slope increases slowly from the centre to a region close to the end of the contact area. Then, it rises rapidly. This can be more easily seen in Fig. 10b where the curvature is plotted. There is a peak of maximum curvature around the end of the contact area—the edge of the contact interface—that suggests the presence of a sharp edge. This can be related to the fact that the junction between the adapted profile and a residual of the initial profile is at a_c.

This figure also shows the profiles and curvatures of logarithmic profile (constructed based on Lundberg's equations [18–20, 51, 52]) and of a circular profile. Again, we can see similarities between our profile and logarithmic profiles. As we can see, the Lundberg profile curvature is also low at the middle and with a sharp peak at the edges. The contact interface using $\upsilon = 3.6$ also presents this affinity.

6.5. Influence of the initial geometry

To further investigate the response of the design process, the initial geometry was changed. More precisely, the initial contact pressure distribution. Fig. 11 shows the evolution of the contact

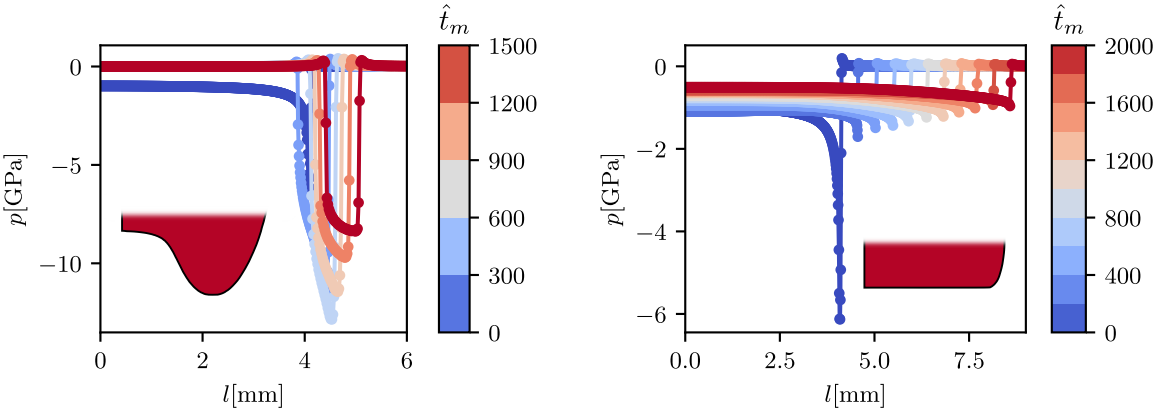

Figure 11: Evolution (from blue to red lines) of the contact pressure along the contact line in scenario IV with $\tau^*_{\text{lim}} = \sigma^*_{\text{lim}} = 0.5$ and the rectangular initial geometry. $\upsilon = 3.6$ in (a) and $\upsilon = 7.1$ in (b). l refers to arc length and the red shapes refer to the geometry of the last iteration.

pressure for a rectangular initial geometry and $\tau^*_{\text{lim}} = \sigma^*_{\text{lim}} = 0.5$. In Fig. 11a $\upsilon = 3.6$ and in Fig. 11b $\upsilon = 7.1$. Although the results seem different from what happened with the circular initial geometry, in reality, the influence of the growth force is the same. For $\upsilon = 3.6$, the point of initial maximum pressure defines the region where the pressure will be concentrated. Thus, a protuberance around this region appears. In contrast, since for $\upsilon = 7.1$ the edge effect slightly dominates, the domain grows as in Fig. 9b. Therefore, for applications where a uniform contact pressure is desirable, it is better to set the initial geometry such that the initial contact pressure distribution has its maximum centred.

6.6. Change of material properties and deformation model

To study the applicability of the growth function, we defined other cases of study modifying the material properties, the shape of Ω_2, the magnitude of the load, and the two–dimensional model. We tested such modifications using the growth function with $\sigma^*_{\text{lim}} = \tau^*_{\text{lim}} = 0.5$ and $\upsilon = 7.1$.

For the plane–stress case, in Fig. 12, we can see the evolution of the contact pressure with $\sigma^*_{\text{lim}} = \tau^*_{\text{lim}} = 0.5$ and $\upsilon = 7.1$. As we can see, the contact area is enlarged while the contact pressure becomes uniform, reaching a value of pressure distribution quality of $Q_p = 0.98$. Similarly to the previous case (Fig. 9b), the maximum pressure is located at the edge.

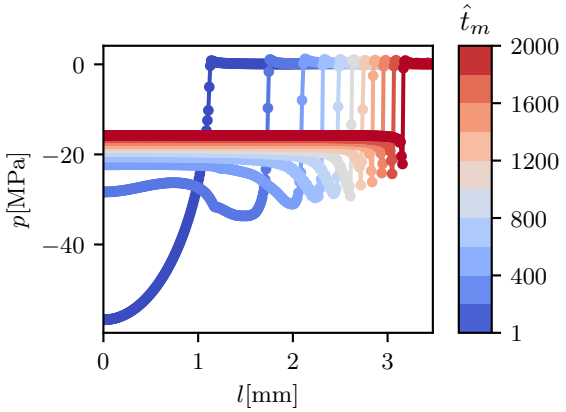

Figure 12: Evolution (from blue to red lines) of the contact pressure along the contact line for the plane–stress case with $\upsilon = 7.1$. l refers to arc length.

With respect to the axisymmetric case, in Fig. 13, we can see the results of the growth process with $\sigma^*_{\text{lim}} = \tau^*_{\text{lim}} = 0.5$ and $\upsilon = 7.1$. Fig. 13a shows the shape of Ω_1 in the coordinate system defined by $\boldsymbol{l}$ and $\boldsymbol{n}$ drawn in Fig. 4. Interestingly, the profile is also similar to Lundberg's profile as can be seen in Fig. 10a. In addition, as seen in Fig. 13b, the contact area was also enlarged, and the contact pressure distribution was improved. In addition, we obtained a high value of pressure distribution quality at the last iteration, $Q_p = 0.97$.

Although the number of examples presented is not enough to definitely conclude about the response of the model, they show a tendency to generate contact interfaces with uniform pressure. This is an important insight since we consider that the efficacy of the bio–inspired generative design cannot be sensitive to the parameters of the growth function. In other words, we consider that the response of the design process seen in Fig. 8 is representative for situations different to the one described in Section 4.

In terms of material properties, the model can be extended to improve the growth phenomenon or to use more complex materials. For the former, it is possible to add a viscous stress tensor similar to the one present in [42] to model cell migration. Such a tensor would directly introduce time dependence. Nonetheless, it could represent an unnecessary cost for a methodology to generate shapes adapted to their loading environments. Further, additional parameters—shear and bulk viscosities—would be introduced. Regarding more complex materials, it would be interesting to

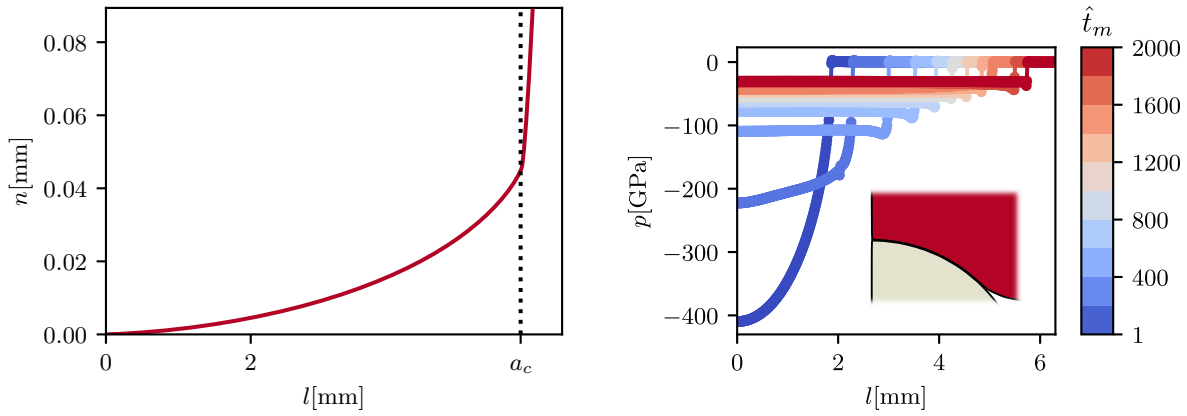

(a) (b)

Figure 13: Results of the axisymmetric case with $\upsilon = 3.6$ after the growth process. (a) shows the contact interface of the last geometry in the coordinate system $\boldsymbol{l}$ and $\boldsymbol{n}$ seen in Fig. 4 and (b) shows the evolution (from blue to red) of the contact pressure (l refers to arc length). The red shape refers to the geometry of the last iteration.

study the process response adding plasticity. In addition, in line with bio–inspiration from synovial joints and considering the increasing development of cartilage–inspired materials with poroelastic properties [53], the use of poroelastic constitutive laws may be of interest.

6.7. Response of the design process after adding another design requirement

In the previous results, since there were no restrictions for the design process, only the evolution of the contact pressure distribution was evaluated regardless of the profile length. In contrast, in this section a restriction to the maximum shear stress is also present; thus, the ~~contact length is fixed.~~ length of the contact profile reaches a stable value.

The design algorithm was set with $\tau^*_{\text{lim}} = \sigma^*_{\text{lim}} = 0.5$, $\upsilon = 7.1$, $\tau_{\text{ref}} = 1.0$MPa, $\alpha_g = \alpha_r = 1.25$, $F = 10$kN and the circular initial geometry. Figs. 14a to 14c show the evolution of the performance variables along the design procedure—the maximum contact pressure and von Mises shear stress, the contact area and the contact pressure and von Mises shear stress qualities—and Fig. 14d indicates the distribution of the contact pressure along the design iterations.

As we can see, the contact interface changes rapidly at the beginning and, once Q_p and Q_v are close to 1, the evolution slows down. For this shape: $\max(|p_c|) = 1.749$GPa, $\max(\sigma_v) = 0.999$GPa, $a_c = 3.369$mm, $Q_p = 0.96$ and $Q_v = 1.001$. Fig. 14 shows that the design process is able to satisfy

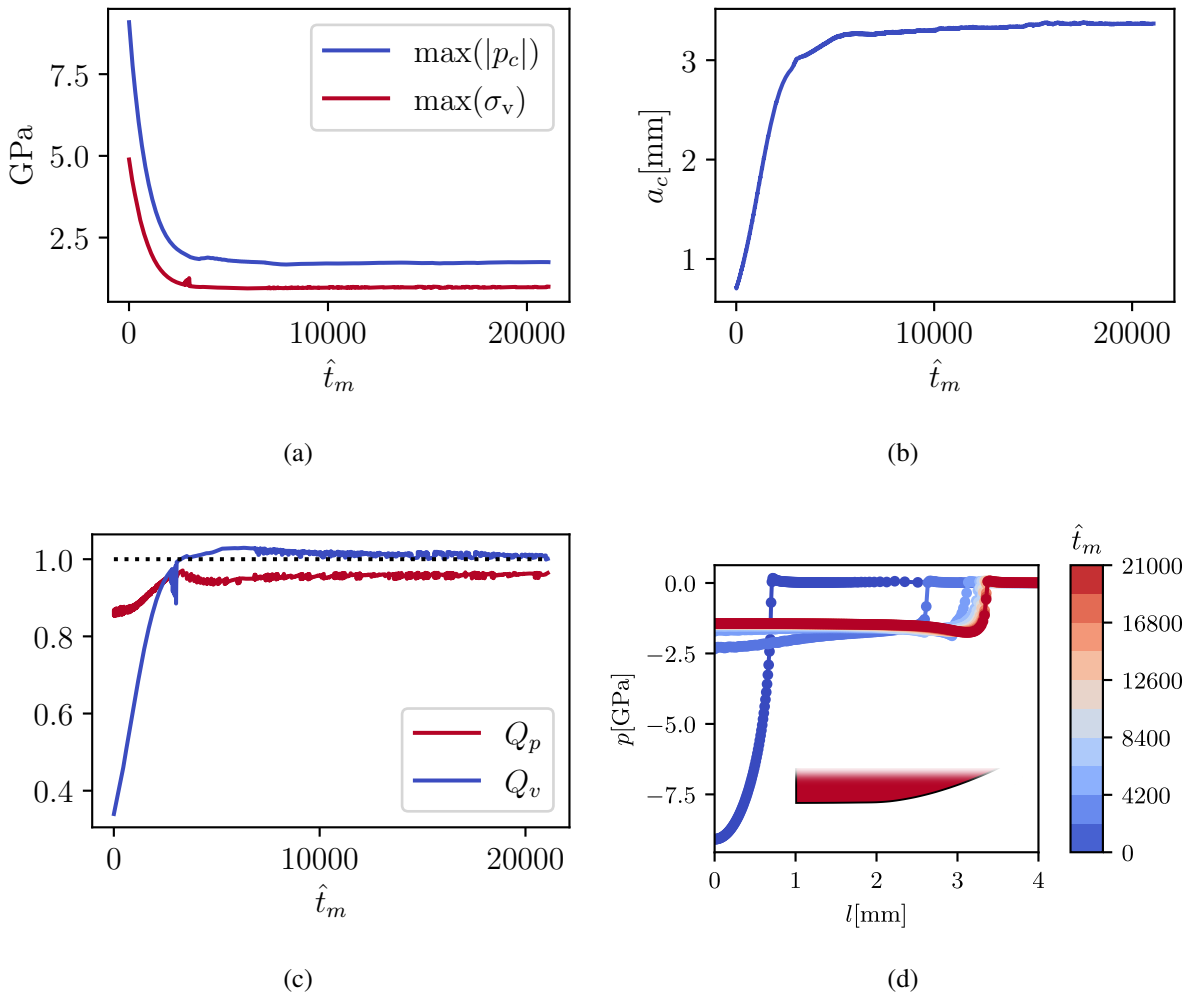

Figure 14: Performance of the contact interface along the design procedure. (a) Evolution of maximum contact pressure and von Mises stress. (b) Evolution of the contact area. (c) Evolution of the contact pressure and von Mises stress qualities. (d) Evolution (from blue to red lines) of the contact pressure along the contact line for the design case. l refers to arc length and the red shape refers to the last iteration.

the restriction and makes the contact pressure uniform. This result demonstrates that the process of synovial joint morphogenesis can be adapted to engineering applications

Nonetheless, the shape of the contact pressure is slightly different (see Figs. 9b and 14d). The edge effect is rounded by applying the restriction term. This means that $\boldsymbol{\sigma}_r$ also affects the distribution of the contact pressure. In addition, $\boldsymbol{\sigma}_g$ also modifies the contact area. Thus, it would be interesting to separate the role of each term. In other words, it would be convenient to define $\boldsymbol{\sigma}_g$ and $\boldsymbol{\sigma}_r$ such that the former would only affect the contact pressure distribution while the latter would only modify the contact area.

6.8. Comparison with other works

The results presented show that the proposed model generates high quality contact interfaces (in terms of contact pressure distribution). We obtained values of Q_p between 0.96 and 0.98. As can be seen in Table 3, only the works presented in [19, 26] are superior in terms of Q_p (see Table 3). Nonetheless, in [19], the methodology is defined only for contact against flat geometries. The work presented in [26] can be applied to curved geometries. However, its design variable is not the shape of the contact interface but the material distribution; hence, the potential engineering applications are not the same than those of the present work.

7. Conclusion

In this work, we studied the impact of applying the rules of synovial joint morphogenesis on the generative design of contact interfaces. For that, we implemented them in an algorithm that mimics synovial joint growth under engineering conditions in an iterative manner. The output of the generative design process is a contact interface adapted to the loading conditions.

The obtained contact interfaces provided a uniform pressure distribution. Such interfaces were achieved following this stress–adaptive rule: growth is proportional to compressive stress, but it is inhibited at regions with high shear stress or high compressive stress. The results showed that the rule works well under different two–dimensional situations (plane–strain, plane–stress and axisymmetric conditions), with different material properties and under different loading conditions. Further, the results also showed that the adaptation process can be applied against curved surfaces. Furthermore, it is possible to control the size of the contact interface by an additional rule that

promotes a global expansion (contraction) when the maximum shear stress is higher (lower) than a given requirement.

The proposed model differs from those present in the literature since it does not require the initial geometry to be close to the final solution, which is an important characteristic in terms of generative design.

Nonetheless, we acknowledge that our work has some limitations. The present work focuses on the contact interface and does not deal with the shape of the free boundary. In addition, as, so far, the current algorithm has only been implemented for frictionless and linear elastic conditions, we cannot conclude about the direct applicability of the model outside these conditions.

Future work is required to continue developing the proposed generative design process. It is necessary to determine appropriate criteria to define the shape of the free boundaries. It would be interesting to study the behaviour of the bio–inspired growth process in applications with dynamic loads or with friction and lubrication. Additionally, more biological processes could be mimicked. For example, it might be interesting to explore the advantages of mimicking the hardening effect during the ossification process or the definition of an anisotropic growth tensor—for instance, one taking into account the direction of the principal strains.

Finally, the results presented here demonstrate that synovial joint morphogenesis can be adapted to generative design in engineering.

Acknowledgements

This research was supported by the French Research National Agency (ANR) Grant No. ANR-20-CE10-0008.

References

[1] A. Neville, A. Morina, T. Liskiewicz, and Y. Yan, "Synovial joint lubrication — does nature teach more effective engineering lubrication strategies?," *Proceedings of the Institution of Mechanical Engineers, Part C: Journal of Mechanical Engineering Science*, vol. 221, no. 10, pp. 1223–1230, 2007.

[2] G. L. Galea, M. R. Zein, S. Allen, and P. Francis-West, "Making and shaping endochondral and intramembranous bones," *Developmental Dynamics*, vol. 250, no. 3, pp. 414–449, 2021.

[3] C. A. Shea, R. A. Rolfe, and P. Murphy, "The importance of foetal movement for co-ordinated cartilage and bone development in utero," *Bone & Joint Research*, vol. 4, no. 7, pp. 105–116, 2015.

[4] N. Felsenthal and E. Zelzer, "Mechanical regulation of musculoskeletal system development," *Development*, vol. 144, no. 23, pp. 4271–4283, 2017.

[5] D. Docheva, C. Popov, P. Alberton, and A. Aszodi, "Integrin signaling in skeletal development and function," *Birth Defects Research Part C*, vol. 102, no. 1, pp. 13–36, 2014.
[6] R. L.-Y. Sah, Y.-J. Kim, J.-Y. H. Doong, A. J. Grodzinsky, A. H. K. Plass, and J. D. Sandy, "Biosynthetic response of cartilage explants to dynamic compression," *Journal of Orthopaedic Research*, vol. 7, no. 5, pp. 619–636, 1989.
[7] M. J. Palmoski and K. D. Brandt, "Effects of static and cyclic compressive loading on articular cartilage plugs in vitro," *Arthritis & Rheumatism*, vol. 27, no. 6, pp. 675–681, 1984.
[8] G. S. Beaupré, S. S. Stevens, and D. R. Carter, "Mechanobiology in the development, maintenance, and degeneration of articular cartilage," *Journal of rehabilitation research and development*, vol. 37, no. 2, p. 145, 2000.
[9] D. R. Carter and M. Wong, "The role of mechanical loading histories in the development of diarthrodial joints," *Journal of Orthopaedic Research*, vol. 6, no. 6, pp. 804–816, 1988.
[10] A. F. Carrera-Pinzón, K. Márquez-Flórez, R. H. Kraft, S. Ramtani, and D. A. Garzón-Alvarado, "Computational model of a synovial joint morphogenesis," *Biomechanics and Modeling in Mechanobiology*, vol. 19, no. 5, pp. 1389–1402, 2020.
[11] M. Giorgi, A. Carriero, S. J. Shefelbine, and N. C. Nowlan, "Mechanobiological simulations of prenatal joint morphogenesis," *Journal of Biomechanics*, vol. 47, no. 5, pp. 989–995, 2014.
[12] S. M. Sadeghian, F. D. Shapiro, and S. J. Shefelbine, "Computational model of endochondral ossification: Simulating growth of a long bone," *Bone*, vol. 153, 2021.
[13] J. A. Tichy and D. M. Meyer, "Review of solid mechanics in tribology," *International Journal of Solids and Structures*, vol. 37, no. 1, pp. 391–400, 2000.
[14] K. Kato, "Classification of wear mechanisms/models," *Proceedings of the Institution of Mechanical Engineers, Part J: Journal of Engineering Tribology*, vol. 216, no. 6, pp. 349–355, 2002.
[15] V. L. Popov, "Wear," in *Contact Mechanics and Friction. Physical Principles and Applications*, ch. 17, pp. 271–284, Springer Berlin, Heidelberg, 2010.
[16] G. Lundberg, "Elastische berührung zweier halbraüme," *Forschung auf den Gebiete des Ingenieurwesen*, vol. 10, pp. 201–211, 1939.
[17] K. L. Johnson, *Contact mechanics*. Cambridge university press, 1985.
[18] P. Johns and R. Gohar, "Roller bearings under radial and eccentric loads," *Tribology International*, vol. 14, no. 3, pp. 131–136, 1981.
[19] L. Cui and Y. He, "A new logarithmic profile model and optimization design of cylindrical roller bearing," *Industrial Lubrication and Tribology*, vol. 67, no. 5, pp. 498–508, 2015.
[20] E. Bergseth and S. Björklund, "Logarithmical Crowning for Spur Gears," *Strojniški vestnik - Journal of Mechanical Engineering*, vol. 56, no. 4, pp. 239–244, 2010.
[21] Y. Liu, M. Chen, L. Yu, L. Wang, and Y. Feng, "Influence of material parameters on the contact pressure characteristics of a multi-disc clutch," *Materials*, vol. 14, no. 21, p. 6391, 2021.
[22] Q. Lin, N. Yang, J. Hong, L. Liu, and Y. Zhang, "An optimization design of contact interface material stiffness for improving the uniformity of the contact pressure," *Journal of Tribology*, vol. 142, no. 6, 2020.
[23] Y. Zhou, Q. Lin, W. Li, T. Yue, J. Yan, and J. Hong, "Optimization of elastoplastic behavior of contact interface for improved contact stress distribution," *Mechanics of Advanced Materials and Structures*, vol. 0, pp. 1–11, 2022.
[24] Y. Wei, Y. Qin, R. Balendra, and Q. Jiang, "FE analysis of a novel roller form: a deep end-cavity roller for roller-type bearings," *Journal of Materials Processing Technology*, vol. 145, no. 2, pp. 233–241, 2004.
[25] H. Kristiansen, K. Poulios, and N. Aage, "Topology optimization for compliance and contact pressure distribution in structural problems with friction," *Computer Methods in Applied Mechanics and Engineering*, vol. 364, p. 112915, 2020.
[26] Q. Lin, Y. Zhou, N. Yang, J. Hong, and C. Wang, "Design of component structure in assemblies for simultaneously regulating contact pressure distribution and natural frequencies," *European Journal of Mechanics - A/Solids*, vol. 94, p. 104557, 2022.
[27] N. Tala-Ighil, P. Maspeyrot, M. Fillon, and A. Bounif, "Effects of surface texture on journal-bearing characteristics under steady-state operating conditions," *Proceedings of the Institution of Mechanical Engineers, Part J:*

Journal of Engineering Tribology, vol. 221, no. 6, pp. 623–633, 2007.
[28] D. Xu, J. Zhang, H. Li, J. Lu, Q. Fan, and H. Dong, "Research on surface topography wear of textured work roll in cold rolling," *Industrial Lubrication and Tribology*, vol. 67, no. 3, pp. 269–275, 2015.
[29] J. Zhao, Z. Li, H. Zhang, and R. Zhu, "Effect of micro-textures on lubrication characteristics of spur gears under 3d line-contact EHL model," *Industrial Lubrication and Tribology*, vol. 73, no. 9, pp. 1132–1145, 2021.
[30] D. Hilding, B. Torstenfelt, and A. Klarbring, "A computational methodology for shape optimization of structures in frictionless contact," *Computer Methods in Applied Mechanics and Engineering*, vol. 190, no. 31, pp. 4043–4060, 2001.
[31] I. Páczelt and Z. Mróz, "Optimal shapes of contact interfaces due to sliding wear in the steady relative motion," *International Journal of Solids and Structures*, vol. 44, no. 3-4, pp. 895–925, 2007.
[32] H. Ou, B. Lu, Z. S. Cui, and C. Lin, "A direct shape optimization approach for contact problems with boundary stress concentration," *Journal of Mechanical Science and Technology*, vol. 27, pp. 2751–2759, 2013.
[33] M. Najjari and R. Guilbault, "Formula derived from particle swarm optimization (PSO) for optimum design of cylindrical roller profile under EHL regime," *Mechanism and Machine Theory*, vol. 90, pp. 162–174, 2015.
[34] M. Duchemin, C. Tugui, and V. Collee, "Optimization of contact profiles using super-ellipse," *SAE International Journal of Materials and Manufacturing*, vol. 10, no. 2, pp. 234–244, 2017.
[35] D. Sysaykeo, E. Mermoz, and T. Thouveny, "Clearance and design optimization of bio-inspired bearings under off-center load," *CIRP Annals*, vol. 69, no. 1, pp. 121–124, 2020.
[36] B. D. Upadhyay, S. S. Sonigra, and S. D. Daxini, "Numerical analysis perspective in structural shape optimization: A review post 2000," *Advances in Engineering Software*, vol. 155, p. 102992, 2021.
[37] S. Arroyave-Tobon, K. Marquez-Florez, P. Heymann, and J.-M. Linares, "Generative design of joint contact surfaces inspired by biological morphogenesis," *CIRP Annals*, vol. 71, no. 1, pp. 125–128, 2022.
[38] K. Marquez-Florez, S. Arroyave-Tobon, and J.-M. Linares, "From biological morphogenesis to engineering joint design: A bio-inspired algorithm," *Materials & Design*, vol. 225, p. 111466, 2023.
[39] P. Wriggers, "Contact kinematics," in *Computational Contact Mechanics*, ch. 4, pp. 56–67, Springer Berlin, Heidelberg, 2006.
[40] M. A. Lewis and J. D. Murray, "Analysis of stable two-dimensional patterns in contractile cytogel," *J Nonlinear Sci*, vol. 1, p. 289–311, 1991.
[41] A. Stéphanou, M. A. J. Chaplain, and P. A. Tracqui, "A mathematical model for the dynamics of large membrane deformations of isolated fibroblasts," *Bull. Math. Biol.*, vol. 66, p. 1119, 2004.
[42] L. Murphy and A. Madzvamuse, "A moving grid finite element method applied to a mechanobiochemical model for 3d cell migration," *Applied Numerical Mathematics*, vol. 158, pp. 336–359, 2020.
[43] Z. Ge, Y. Hu, B. C. Heng, Z. Yang, H. Ouyang, E. H. Lee, and T. Cao, "Osteoarthritis and therapy," *Arthritis Care & Research*, vol. 55, no. 3, pp. 493–500, 2006.
[44] M. Rakhsha, C. R. Smith, A. M. Recuero, S. C. E. Brandon, M. F. Vignos, D. G. Thelen, and D. Negrut, "Simulation of surface strain in tibiofemoral cartilage during walking for the prediction of collagen fibre orientation," *Computer Methods in Biomechanics and Biomedical Engineering: Imaging & Visualization*, vol. 7, no. 4, pp. 396–405, 2019.
[45] Electricité de France, "Finite element *code_aster*, analysis of structures and thermomechanics for studies and research." Open source on `www.code-aster.org`, 1989–2017.
[46] C. Geuzaine and J.-F. Remacle, "Gmsh: A 3-d finite element mesh generator with built-in pre- and post-processing facilities," *International Journal for Numerical Methods in Engineering*, vol. 79, no. 11, pp. 1309–1331, 2009.
[47] L. Mattei and F. Di Puccio, "Frictionless vs. Frictional Contact in Numerical Wear Predictions of Conformal and Non-conformal Sliding Couplings," *Tribology Letters*, vol. 70, no. 4, p. 115, 2022.
[48] S. Axler, "Hilbert spaces," in *Measure, Integration & Real Analysis. Graduate Texts in Mathematics*, ch. 8, pp. 211–254, Springer Cham, 2020.
[49] A. Ruggiero and A. Sicilia, "Implementation of a finite element deformation model within an elasto-hydrodynamic lubrication numerical solver for a ball in socket tribopair," *Frontiers in Mechanical Engineering*, vol. 8, 2022.
[50] J. Girard, "Femoral head diameter considerations for primary total hip arthroplasty," *Orthopaedics & Trauma-*

tology: Surgery & Research, vol. 101, no. 1, Supplement, pp. S25–S29, 2015.

[51] C. Huang, Y. Zhao, and M. Liu, "Analytical modeling and optimization of logarithmic sprag clutch considering profile modification," *Shock and Vibration*, vol. 2018, pp. 1–13, 2018.

[52] H. Duan, Q. Yu, and Z. Wang, "Design of logarithmic crowned roller for tapered roller bearings based on the elastohydrodynamic lubrication model," *Industrial Lubrication and Tribology*, vol. 73, no. 5, pp. 742–749, 2021.

[53] N. Raske, S. Soltanahmadi, G. de Boer, M. Bryant, and R. Hewson, "Finite element investigations of the fluid-solid behaviour in a bio-inspired poroelastic bearing," *Proceedings of the Institution of Mechanical Engineers, Part J: Journal of Engineering Tribology*, vol. 236, no. 8, pp. 1531–1544, 2022.